Heat transfer model and finite element formulation for simulation of selective laser melting

Souvik Roy, Mario Juha, Mark S. Shephard & Antoinette M. Maniatty
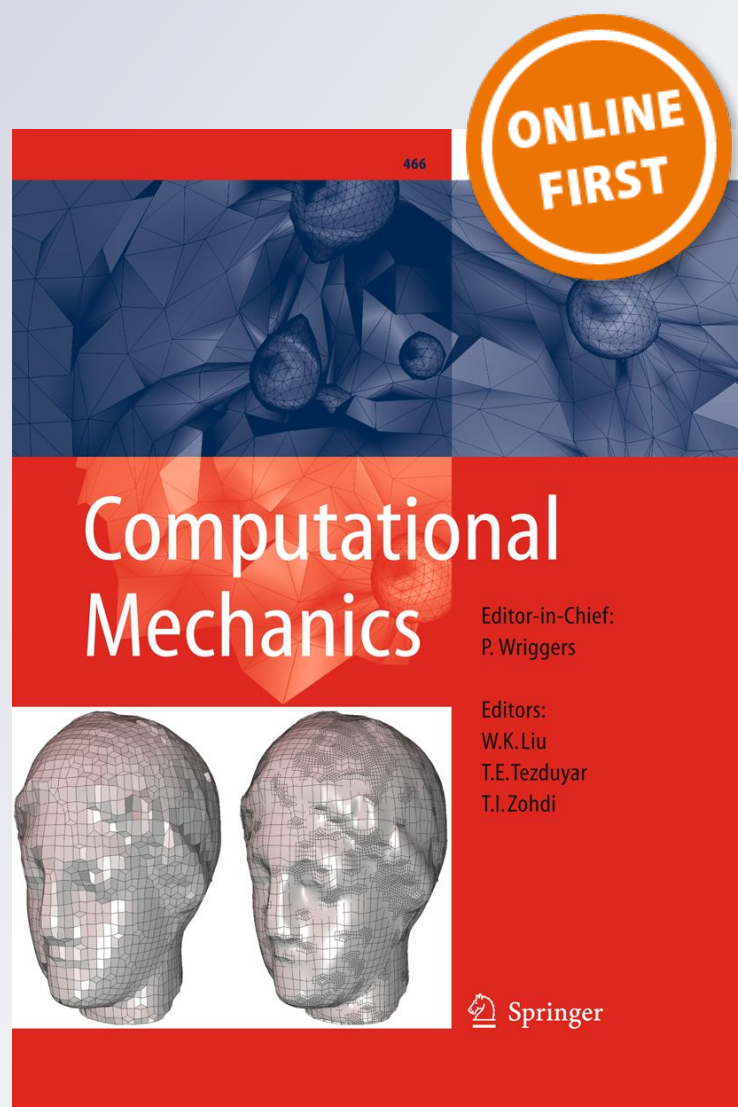
466

ONLINE FIRST

Computational Mechanics

Editor-in-Chief:
P. Wriggers

Editors:
W.K. Liu
T.E. Tezduyar
T.I. Zohdi

🦄 Springer

🦄 Springer

CrossMark

ORIGINAL PAPER

Heat transfer model and finite element formulation for simulation of selective laser melting

Souvik Roy[1] · **Mario Juha[1,2]** · **Mark S. Shephard[1]** · **Antoinette M. Maniatty[1]**

Abstract A novel approach and finite element formulation for modeling the melting, consolidation, and re-solidification process that occurs in selective laser melting additive manufacturing is presented. Two state variables are introduced to track the phase (melt/solid) and the degree of consolidation (powder/fully dense). The effect of the consolidation on the absorption of the laser energy into the material as it transforms from a porous powder to a dense melt is considered. A Lagrangian finite element formulation, which solves the governing equations on the unconsolidated reference configuration is derived, which naturally considers the effect of the changing geometry as the powder melts without needing to update the simulation domain. The finite element model is implemented into a general-purpose parallel finite element solver. Results are presented comparing to experimental results in the literature for a single laser track with good agreement. Predictions for a spiral laser pattern are also shown.

Keywords Selective laser melting · Finite element simulation · Consolidation · Melt pool size · Additive manufacturing

1 Introduction

Additive Manufacturing (AM), where three-dimensional (3D) objects are created from a digital model by depositing and fusing successive layers of material, provides the ability to produce low-volume, customized products with complex geometries relatively quickly at a moderate cost. These processes have the potential to significantly impact a wide array of applications. AM of metallic materials, typically a powder-bed process with a laser or e-beam power source to fuse the material, requires substantial research and development before the process can be used reliably. A primary barrier to the broader use of powder-bed AM processes is the inability to predict the quality, in terms of geometric accuracy and material properties, for any given part [1].

Process simulation can help to navigate the complex process–structure–property relations. The first step in modeling the process is predicting the temperature and solid–liquid phase fields during the process, which can then be used subsequently in thermal–mechanical and material microstructure evolution simulations to predict the residual stresses, distortion, and material properties. In this work, the focus is on the selective laser melting (SLM) powder-bed processes, where a layer of powder is deposited with a roller and then melted with a laser to build each layer of a part.

Developing both the model and the required simulation tools to accurately predict the temperature and phase history in SLM is challenging. The model needs to properly consider the interaction of the laser with the powder as it melts, the consolidation of the powder, and the solid–liquid phase change. The problem is computationally challenging because of the complexity of the model and the multi-scale nature of the process. The melting and re-solidification process occurs on a scale of 10 s of μm while the part scale is on the cm scale, and parts are typically composed of thousands

✉ Antoinette M. Maniatty
maniaa@rpi.edu

1 Department of Mechanical, Aerospace, and Nuclear Engineering, Rensselaer Polytechnic Institute, Troy, NY 12180, USA

2 Present Address: Programa de Ingeniería Mecánica, Universidad de La Sabana, Campus del Puente del Común, Chía, Colombia

 Springer

of layers. Furthermore, the temperature history at any given location in the part, necessary to predict residual stresses and microstructure, can only be determined by modeling the layer-by-layer process. Thus, efficient, scalable simulation tools are needed.

There has been significant effort in recent year to develop models to predict the temperature field, melting, and re-solidification during powder-based AM processes. That work has considered various scales, from the powder particles to the complete part [2]. At the mesoscale, there has been some effort to model the heating, melting, and coalescence of individual powder particles [3–6]. Other work treats the powder as a continuum and models the local melting in the vicinity of the laser in a single layer or a few layers [7–10]. At the larger scale, 3D thermal–mechanical finite element models have been used to predict residual stresses and distortion in plates [11–13] and warping during the build of simple parts [14,15].

The focus of this work is modeling the heating, melting and re-solidification for a laser track in a single layer during the build process, in order to capture accurately the effect of the laser path on the thermal history, which has been found to significantly affect part quality [16]. The laser heating model presented in Gusarov et al. [7] and extended by Verhaeghe et al. [8] has been shown to predict melt zones consistent with experiments [7,8,17] involving a single laser track. Gusarov et al. [7] solved the radiative transfer equation taking into consideration isotropic scattering of the laser beam in the powder bed in order to define an appropriate heat source model. However, that model was found to predict excessive heating for a given laser power as compared to experiments, and the model does not account for consolidation of the powder as it melts. Verhaeghe et al. [8] extended Gusarov's model to consider vaporization and consolidation in the depth direction by developing an iterative shrinking routine, however, the effect of the consolidation on the laser energy absorbed was not considered. Xiao et al. [18] developed an analytic model of the melting and consolidation of a layer of a powder-bed without a substrate and assuming a constant heat flux at the surface, and predict the one-dimensional porosity distribution.

In this work, we present a novel approach and finite element formulation for modeling the melting, consolidation, and re-solidification process that occurs in SLM. In the model, we introduce two state variables to track the phase (melt/solid) and the degree of consolidation (powder/fully dense). While introducing a phase variable is a common approach for modeling phase change, the consolidation state variable is new. The introduction of the consolidation state variable provides the ability to both predict porosity in the final part and to directly incorporate the effect of consolidation on the material properties, energy absorption, and geometric evolution. These combined effects have not been considered previously in models that treat the powder as a

continuum. The material properties naturally depend on the state variables. In addition, we model how the degree of consolidation impacts the absorption of the laser energy into the material as it transforms from a porous powder to a dense melt. A Lagrangian finite element formulation, which solves the governing equations on the undeformed (unconsolidated) reference configuration is derived, which naturally considers the effect of the changing geometry as the powder melts without needing to update the simulation domain. A transient, fully implicit integration algorithm is used allowing for relatively large time steps. The finite element model is implemented into the general-purpose parallel finite element solver Albany developed by the Computational Multiphysics Department at Sandia National Laboratories [19], which allows for scalable parallel computing on high performance computing platforms.

This paper is organized as follows. Section 2 contains the governing equations that describes the transient heat transfer model with phase change, consolidation, and a laser heat source. In Sect. 3, the Lagrangian finite element formulation accounting for the evolving geometry due to consolidation is presented. Section 4 presents the simulation results where the effect of consolidation on the model is presented, the efficiency of the model is demonstrated, comparison with existing experimental results available in the literature is shown, and results for a realistic laser path are also presented. Lastly, conclusions are drawn and summarized.

2 Model equations for powder-based metal additive manufacturing

Powder-based metal additive manufacturing involves using a directed laser or e-beam to melt a pattern in a thin powder layer that condenses and solidifies onto a dense, solid substrate (Fig. 1). The path of the beam can be defined in terms of the beam center (x_c, y_c) on the surface of the powder layer as a function of time t. To distinguish the powder from the fully dense phase and the liquid from the solid, we introduce two state variables, $0 \leq \psi, \phi \leq 1$, where ψ is the consolidation parameter with $\psi = 1$ in the fully dense region and $\psi = 0$ in the powder, and ϕ is the phase parameter, with $\phi = 1$ in the fully melted region and $\phi = 0$ in the fully solid region.

2.1 Energy balance

Letting Ω be bounded by Γ represent the region of interest, the boundary value problem consists of the first law of thermodynamics, an equation for the energy density e in terms of the temperature T and material state variables, and the usual temperature and flux boundary and initial conditions.

$$\frac{de}{dt} - \text{grad} \cdot \left[k(\psi) \, \text{grad}(T) \right] - U(\psi, \boldsymbol{x}, t) = 0 \quad \text{in } \Omega \qquad (1)$$
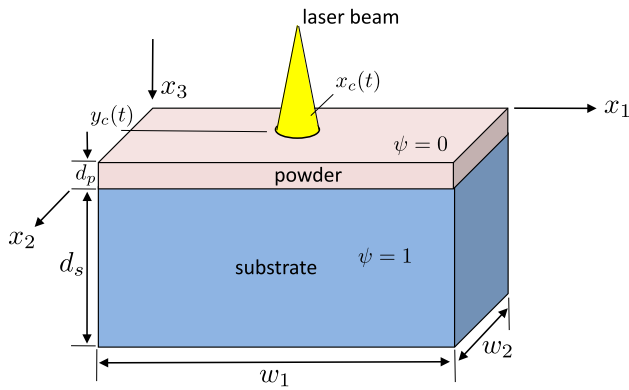
Fig. 1 Powder-based metal additive manufacturing process diagram

$$e = C_s(\psi)T + p(\phi)\{L + [C_l - C_s(\psi)](T - T_m)\} \quad \text{in } \Omega \quad (2)$$

$$T = \hat{T} \quad \text{on } \Gamma_1 \quad (3)$$

$$[k(\psi)\,\text{grad}(T)] \cdot \boldsymbol{n} = \hat{q} \quad \text{on } \Gamma_2 \quad (4)$$

$$T(\boldsymbol{x}, 0) = T_0(\boldsymbol{x}) \quad \text{in } \Omega \quad (5)$$

where k is the thermal conductivity, U is the heat source (power density) distribution delivered from the beam into the material, C_s and C_l are the volumetric heat capacities in the solid and liquid, respectively, L is the latent heat of fusion/melting, and T_m is the average melt temperature, which we take to be the average of the liquidus (T_l) and solidus (T_s) temperatures. Furthermore, $\hat{T}$ is the temperature specified on the part of the boundary Γ_1, $\hat{q}$ is the heat flux into the part of the boundary Γ_2, $\Gamma_1 \cup \Gamma_2 = \Gamma$ and $\Gamma_1 \cap \Gamma_2 = \emptyset$, and $\boldsymbol{n}$ is the outward unit normal on Γ. The function $p(\phi)$ in Eq. (2) is defined following the thermodynamically consistent phase-field approach [20] such that $p(0) = 0$ and $p(1) = 1$ and $\frac{dp}{d\phi} = \frac{d^2 p}{d\phi^2} = 0$ at $\phi = 0$ and $\phi = 1$. Specifically, we choose

$$p(\phi) = \phi^3 \left(10 - 15\phi + 6\phi^2\right). \quad (6)$$

The thermal conductivity and heat capacity in the solid depend on the degree of consolidation characterized by ψ. The thermal conductivity is taken to be

$$k(\psi) = (1 - \psi)k_p + \psi k_d \quad (7)$$

where k_p and k_d are the thermal conductivity in the powder and dense material, respectively. The volumetric heat capacity in the solid depends on the porosity ε, which in turn, depends on the consolidation ψ. Letting ε_0 be the initial porosity of the powder and C_d be the heat capacity of the fully dense material, then

$$\varepsilon = \varepsilon_0(1 - \psi) \quad (8)$$

$$C_s(\psi) = (1 - \varepsilon)C_d = [1 - \varepsilon_0(1 - \psi)]C_d \quad (9)$$

In general, the thermal conductivity and heat capacity are also temperature dependent.

To complete the governing equations, we must still define two additional relationships between the temperature T and the state variables ϕ and ψ, and we must define a functional form of the heat source U absorbed into the material from the laser beam. These will be described in the next two sections.

2.2 State variables

The phase parameter is defined such that $\phi = 0$ if $T < T_s$, $\phi = 1$ if $T > T_l$ and ϕ makes a smooth transition when $T_s \leq T \leq T_l$, the so-called "mushy" region. A functional form that can approximate this behavior is

$$\phi = \frac{1}{2}\left\{\tanh\left[\frac{A(T - T_m)}{T_l - T_s}\right] + 1\right\} \quad (10)$$

where A defines the sharpness of the transition, and setting $A = 5$ generates a smooth transition between the solidus and liquidus temperatures.

To test the validity of using Eq. (10), we compare it to the phase field predicted in the phase-field method. A thermodynamically consistent evolution equation for the phase parameter derived in Wang et al. [20] with the energy density in Eq. (2) yields

$$\tau \frac{d\phi}{dt} = \frac{dp}{d\phi}\left[\left(\frac{L}{T_m} - C_l + C_s\right)\left(1 - \frac{T_m}{T}\right)\right.$$
$$\left. + (C_l - C_s)\ln\left(\frac{T}{T_m}\right)\right] \quad (11)$$
$$- \frac{1}{2a}\phi\left(1 - 3\phi + 2\phi^2\right) + \epsilon^2 \nabla^2 \phi$$

where τ, a, and ϵ are parameters related to the interface thickness δ, interface energy σ, and the interface mobility μ by

$$\tau = \frac{6\sqrt{2}\delta L}{\mu T_m^2}, \quad a = \frac{\sqrt{2}\delta T_m}{12\sigma}, \quad \epsilon^2 = \frac{\delta^2}{a}. \quad (12)$$

The phase-field method is inherently a diffuse interface method, and the interface thickness δ is typically defined in terms of the discretization size, which must be sufficiently large so that the interface can be resolved accurately by the discretization. In the case of alloys, where the liquidus and solidus temperatures are different, the actual interface is diffuse and the interface thickness can be approximately related to the local temperature gradient as simply

$$\delta \approx \frac{T_l - T_s}{|\text{grad}(T)|}. \quad (13)$$

To compare the phase field resulting from the functional form in Eq. (10) and the evolution Eq. (11), consider a
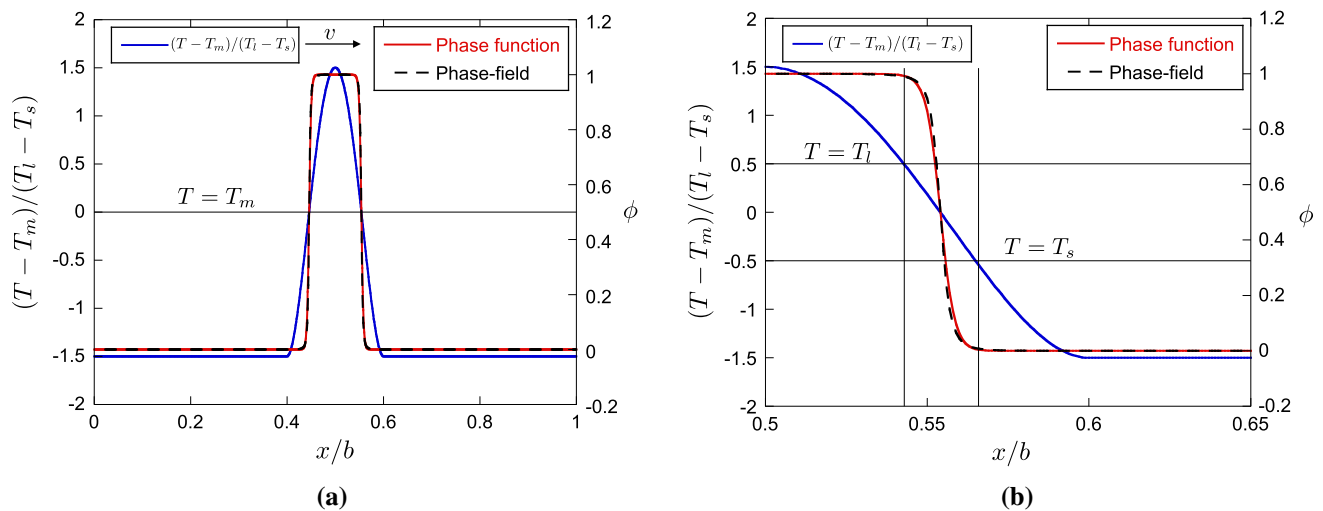
(a)

(b)

Fig. 2 Example comparing phase parameter ϕ computed using the functional form in Eq. (10) (phase function) and using the evolution Eq. (11) (phase-field) for a moving temperature field. Temperature distribution (blue curve) moving left to right. **a** The temperature and phase distributions for entire domain. **b** The transition region from melt to solid ahead of the moving melt interface. (Color figure online)

prescribed, normalized temperature field that varies from below the solidus to above the liquidus temperature in a one-dimensional domain $0 \leq x \leq b$ moving at velocity v such that

$$\frac{T - T_m}{T_l - T_s} = -1.5 + 3H\left[1 - \frac{(x - vt)^2}{h^2}\right]\left[1 - \frac{(x - vt)^2}{h^2}\right]^2 \tag{14}$$

where H is the Heaviside function and $2h$ is the width of the region where the temperature is varied from the baseline temperature (see Fig. 2a). In this example, we set $h = 0.1b$. The interface thickness can then be estimated, averaging the temperature gradient in the region of interest, from Eq. (13) $\delta \approx h/3$. Using this and typical material properties for stainless steel 316L, we compute the parameters in Eq. (12)

$$\tau = 5.78 \times 10^{-6}\frac{Lb}{T_m v}, \quad \frac{1}{a} = 4.36 \times 10^{-5}\frac{L}{T_m},$$

$$\epsilon^2 = 4.75 \times 10^{-8}\frac{Lb^2}{T_m} \tag{15}$$

where Eq. (11) can be non-dimensionalized by multiplying through by T_m/L and using normalized time and space dimensions $\tilde{t} = vt/b$ and $\tilde{x} = x/b$. In addition, we let $C_l = 4.64L/T_m$ and $C_s = 3.31L/T_m$. The resulting phase distributions computed directly from the phase function in Eq. (10) and determined by solving the phase-field evolution Eq. (11) are shown in Fig. 2 on the same graph with the normalized temperature distribution at $\tilde{t} = 0.5$. The resulting phase field from both equations is nearly identical.

Equation (10) gives an accurate representation of the phase field when the time associated with the phase change, that is the time it takes for ϕ to reach a steady-state value ($d\phi/dt = 0$), is very small compared to the time associated with the motion of the melt interface. For stainless steel 316L, the time associated with the melt interface reaching steady-state is on the order of 10^{-6} s. A typical beam velocity is on the order of 100 mm/s, and thus, the distance the beam travels while the melt interface reaches steady-state is of the order 0.1 μm, which is small compared to the typical beam diameter of approximately 100 μm. Thus, it is reasonable to treat the melt interface position as being at steady-state at any instant in time and to use Eq. (10).

Lastly, the consolidation parameter is related directly to the history of the phase parameter and the current state of consolidation. If the powder is fully melted, that is $\phi = 1$ at some point in time, we assume that the material at this location becomes fully dense, and thus $\psi = 1$ at that time and will remain fully dense. If the material is only partially melted, then the peak value of ϕ will be $0 < \phi < 1$. This occurs in alloys in the temperature regime between the solidus and liquidus temperatures or if the full latent heat required for melting is not supplied. If the material was initially powder and is not fully melted, then we assume the material is not fully consolidated, and ψ takes on the peak value of ϕ. Once the material is consolidated, we assume it remains consolidated. Thus, in general, ψ takes on the maximum value of either the current value of ψ or the peak value of ϕ at any time up to the current time at a given location $\boldsymbol{x} \in \Omega$, specifically,

$$\psi(\boldsymbol{x}, t) = \max_{0 \leq t' \leq t}\left[\phi(\boldsymbol{x}, t'), \psi(\boldsymbol{x}, t)\right]. \tag{16}$$

Table 1 ϕ and ψ values at different states of the material

Solid powder	Solid porous	Mushy powder/melt	Liquid melt	Mushy melt/dense	Solid dense
$\phi = 0$	$\phi = 0$	$0 < \phi < 1$	$\phi = 1$	$0 < \phi < 1$	$\phi = 0$
$\psi = 0$	$0 < \psi < 1$	$0 < \psi < 1$	$\psi = 1$	$\psi = 1$	$\psi = 1$

Table 2 Material properties for SS 316L used here [7,21]

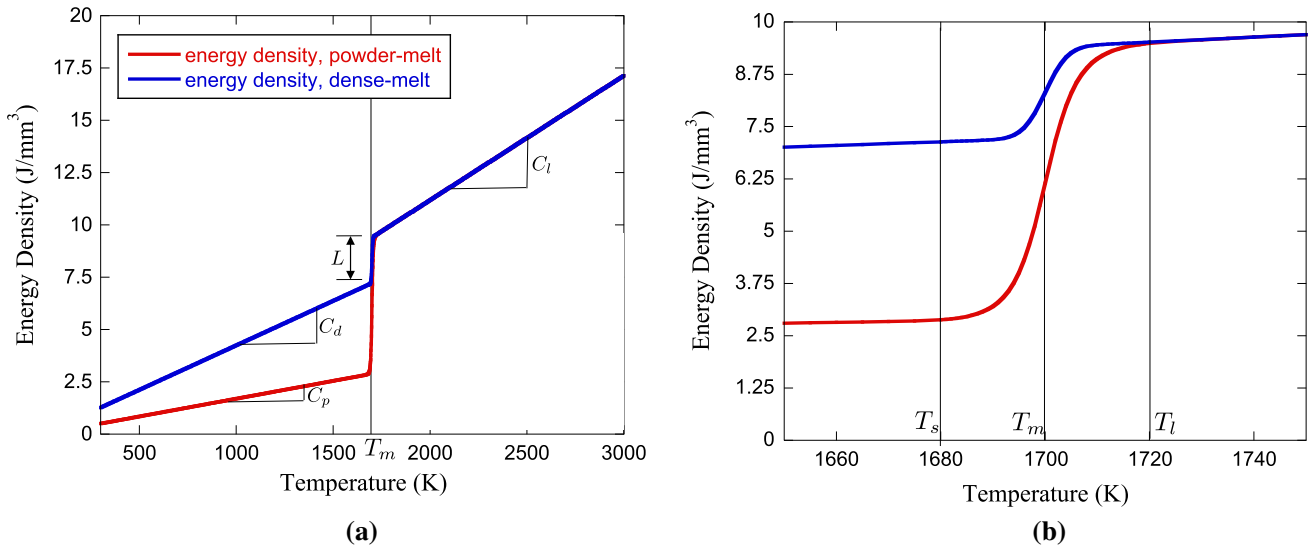| T_s (K)	T_l (K)	$L \left(\frac{J}{mm^3}\right)$	$C_d \left(\frac{J}{mm^3\,K}\right)$	$C_l \left(\frac{J}{mm^3\,K}\right)$	$k_d \left(\frac{W}{mm\,K}\right)$	$k_p \left(\frac{W}{mm\,K}\right)$
1680	1720	2.18	4.25×10^{-3}	5.95×10^{-3}	20×10^{-3}	0.5×10^{-3}

(a)

(b)

Fig. 3 Variation of internal energy density e with temperature: **a** showing the broad temperature range experienced during SLM, and **b** detail showing the phase transition region from solidus T_s to the liquidus T_l temperature. The red curve is for the initially powder material, where the volumetric heat capacity of the powder ($\psi = 0$) is denoted $C_p = (1 - \varepsilon_0)C_d$. The blue curve is for fully consolidated material ($\psi = 1$). (Color figure online)

Table 1 summarizes the relationship between the material state and the two state variables.

Using these state variable definitions, Eqs. (10) and (16), together with Eqs. (6) and (9) in the energy density Eq. (2), we can express the energy density in terms of the temperature history for both initially dense and powder materials. In this work, we consider stainless steel (SS) 316L with the properties listed in Table 2. With those properties, and assuming an initial powder porosity of $\varepsilon_0 = 0.6$, we plot the internal energy density as a function of temperature in Fig. 3. When the powder is heated and transitions to the liquid phase, the energy density increases sharply both because of the latent heat L and because of the consolidation.

2.3 Heating source

The amount of laser power absorbed into the metal, U, changes considerably as the metal transforms from a powder to a fully dense melt, and thus, the heat source term must depend on the consolidation ψ. The intensity of the laser power across the beam diameter is often modeled as a Gaussian distribution and applied on the powder surface [22,23]. However, to accurately predict the melt pool dimensions and the temperature distribution in the vicinity of the laser beam, the penetration of the heat source into the powder and substrate must be considered, which requires treating the heat source as a volume source term rather than surface flux.

We start with the heat source derived by Gusarov et al. [7], who consider laser energy absorption into a scattering medium (powder). That model shows good agreement with experiments in predicting the width of the powder consumed and of the contact region with the remelted substrate material along the laser track, but with a reduction in power in the model as compared to the experiment. From simulations, we find that the powder melts very fast and that for the majority of the time that the laser is heating the material, it is heating a melted region rather than powder. It is estimated that while 70–80% of the laser power is absorbed into the powder due to the porosity and scattering [7], when the material is fully consolidated only 20–60% of the energy is absorbed [24–

26], where the fraction of energy absorbed increases with the laser power [25]. Thus, too much energy is being put into the material if the consolidation is not considered in the laser heat source model, which may account for why Gusarov et al. [7] observed excessive heating in their model. We develop a model for U that transitions from the power density absorbed into a powder to that absorbed by a melt pool, such as in laser welding.

To model the power density absorbed into the powder, U_p, we adopt the model derived in Gusarov et al. [7], which we summarize here for completeness.

$$U_p(\boldsymbol{x}, t) = \beta Q(r(x_1, x_2, t)) h(\xi(x_3)) \tag{17}$$

$$r(x_1, x_2, t) = \sqrt{(x_1 - x_c(t))^2 + (x_2 - y_c(t))^2},$$
$$\xi(x_3) = \beta x_3 \tag{18}$$

$$\beta = \frac{3}{2} \frac{(1 - \varepsilon_0)}{\varepsilon_0 D}, \quad \lambda = \beta d_p \tag{19}$$

$$Q(r) = H(R - r) \frac{3P}{\pi R^2} \left(1 - \frac{r^2}{R^2} \right)^2 \tag{20}$$

$$h(\xi) = H(\lambda - \xi) E \left\{ \frac{2\rho a^2}{C} \left[A \left(b_2 e^{2a\xi} - b_1 e^{-2a\xi} \right) \right. \right.$$
$$\left. - B \left(c_2 e^{-2a(\lambda - \xi)} - c_1 e^{2a(\lambda - \xi)} \right) \right]$$
$$\left. + 3a^2 \left(e^{-\xi} + \rho e^{\xi - 2\lambda} \right) \right\} \tag{21}$$

$$a = \sqrt{1 - \rho}, \quad A = (1 - \rho^2) e^{-\lambda},$$
$$B = 3 + \rho e^{-2\lambda}, \quad E = \frac{1}{3 - 4\rho} \tag{22}$$

$$b_1 = 1 - a, \quad b_2 = 1 + a, \quad c_1 = b_2 - \rho b_1,$$
$$c_2 = b_1 - \rho b_2 \tag{23}$$

$$C = b_1 c_2 e^{-2a\lambda} - b_2 c_1 e^{2a\lambda} \tag{24}$$

where β is the extinction coefficient of the powder bed, which gives a measure of how quickly the radiation intensity attenuates in the material; Q is the radial distribution of the power density in terms of the radial distance r on the surface from the laser center (x_c, y_c) (Fig. 1), the laser power P, and beam radius R; and h is the depth distribution in terms of the scaled depth ξ. Furthermore, D is the average particle powder diameter, d_p is the thickness of the powder bed, and ρ is the hemispherical reflectivity of the powder material in the dense form. The Heaviside function H is used to ensure that the above function is only non-zero for $r \leq R$ and $\xi \leq \lambda$, that is under the laser beam in the powder layer.

The volumetric heating from an incident laser on a substrate is typically assumed to decay exponentially with depth according to the Beer–Lambert law [24]. From Gusarov et al. [7], we also obtain a relationship for the fraction of incident radiation absorbed by the substrate, which we denote g_s,

$$g_s = E \left\{ \frac{\rho a}{C} \left[2a^2 B - A \left(b_1 e^{-2a\lambda} + b_2 e^{2a\lambda} \right) \right] + 3a^4 e^{-\lambda} \right\}. \tag{25}$$

The heating in the substrate, under the powder layer, may then be expressed as

$$U_{sp}(\boldsymbol{x}, t) = \beta Q(r(x_1, x_2, t)) H(\xi - \lambda) g_s f e^{-f(\xi - \lambda)} \tag{26}$$

where f is the rate at which the absorbed energy decays in the substrate, but does not impact the total energy absorbed.

When the material is melted, it becomes fully consolidated, and we would expect the power density absorbed to follow the Beer–Lambert decaying exponential form for the depth profile. The function h in Eq. (21) is very close to a decaying exponential, and the energy absorbed will decrease as the volume decreases. The local volume ratio associated with consolidation is

$$\frac{d\Omega}{d\Omega_0} = \frac{1 - \varepsilon_0}{1 - \varepsilon_0(1 - \psi)} \tag{27}$$

where $d\Omega$ is the local differential consolidated volume and $d\Omega_0$ is the initial unconsolidated differential volume in the powder. Letting $\boldsymbol{x}$ be the particle position in the reference configuration (unconsolidated), we propose that the power density absorbed in the powder/melt per unit unconsolidated material, $d\Omega_0$, accounting for melting, may be expressed as

$$U_{pm}(\boldsymbol{x}, t) = \beta Q(r(x_1, x_2, t)) h(\xi(x_3)) \frac{1 - \varepsilon_0}{1 - \varepsilon_0(1 - \psi)}$$
$$\text{for } x_3 \leq d_p. \tag{28}$$

After the powder has melted, the Beer–Lambert decaying exponential should be a continuous function into the substrate. The power absorbed into the substrate may therefore be expressed generally, for substrate material below powder or melted material, as

$$U_s(\boldsymbol{x}, t) = \beta Q(r(x_1, x_2, t)) \left[g_m \psi^\star + g_s(1 - \psi^\star) \right]$$
$$f e^{-f(\xi - \lambda)} \quad \text{for } x_3 > d_p \tag{29}$$

where $g_m = h(\lambda)/f$ and $\psi^\star = \psi(x_1, x_2, d_p^-)$, that is, $\psi^\star$ is the value of ψ in the initial powder layer immediately above the substrate. Plots of typical depth profiles are shown in Fig. 4 before and after melting. After melting, the fraction of energy absorbed in this example is 42%, which is consistent with the experimental observation in Cremers et al. [25] for laser welding in SS 316. For simplicity and because the material melts very rapidly when the laser passes over a region of the powder, we approximate Eq. (29) letting $\psi^\star = 1$, which approximates the entire region under the laser as being melted instantaneously.
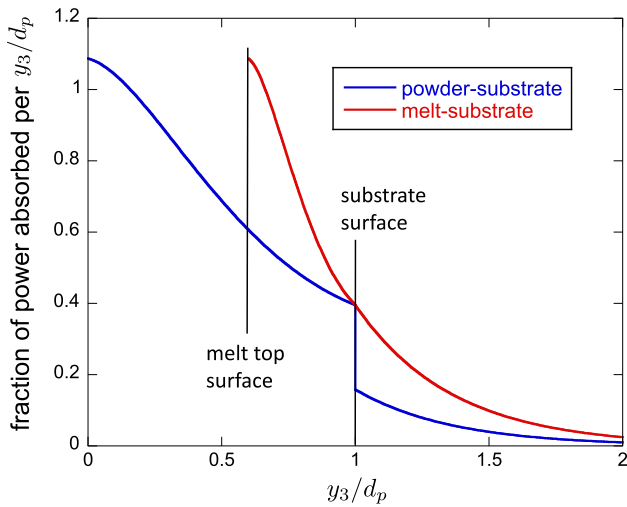
Fig. 4 Depth profile of heat source model showing the fraction of laser power absorbed per unit scaled depth, y_3/d_p, where $d_p = 50\,\mu m$ is the initial powder depth, y_3 is the distance in the depth direction (in deformed/consolidated configuration) from the initial powder top surface. The integral of these curves is total fraction of laser power absorbed. The curves shown are for an initial porosity of 60% with spherical particles of stainless steel 316L of diameter $20\,\mu m$. The initial percent power absorbed into the powder and substrate is 77%, and when fully melted the percent of power absorbed is 42%

3 Parallel finite element implementation

The model described in Sect. 2 has been implemented into the general-purpose, parallel finite element solver Albany developed by the Computational Multiphysics Department at Sandia National Laboratories [19,27], where we use a Lagrangian finite element approach, expressing the weak form of the energy balance equation on the undeformed (unconsolidated) geometry. The usual weak form of the energy balance Eq. (1) on the deformed geometry Ω is

$$\int_{\Omega} \left[k(\mathrm{grad}T) \cdot (\mathrm{grad}w) - Uw + \dot{e}w \right] d\Omega \\ - \int_{\Gamma_2} \hat{q}w \, d\Gamma = 0 \tag{30}$$

where w is an arbitrary weighting function and where the flux boundary condition (4) is incorporated. Noting that

$$\mathrm{grad}T = \boldsymbol{F}^{-1}\nabla T, \quad d\Omega = \det \boldsymbol{F} \, d\Omega_0 \tag{31}$$

where grad and ∇ are the gradient operators with respect to the coordinates in the deformed ($\boldsymbol{y}$) and undeformed ($\boldsymbol{x}$) configurations, respectively, and $\boldsymbol{F} = \nabla \boldsymbol{y}$ is the deformation gradient, we can apply a change of variables to obtain the weak form of the energy balance with respect to the undeformed volume Ω_0. Thus, we have the following non-linear equation that we solve for the temperature field

$$\int_{\Omega_0} \left[k(\boldsymbol{F}^{-1}\nabla T) \cdot (\boldsymbol{F}^{-1}\nabla w) - Uw + \dot{e}w \right] \det \boldsymbol{F} \, d\Omega_0 = 0 \tag{32}$$

where k, U, and e are as defined in Sect. 2. Furthermore, insulated boundary conditions are assumed on all surfaces of the model such that $\hat{q} = 0$. The simulation model domains are created sufficiently large or with symmetry boundaries, such that the insulated boundary conditions on the lateral and bottom surface are appropriate. The SLM process is performed in a vacuum, so there is no convection on the top surface. Furthermore, the time scale of the simulations of the local laser melting are sufficiently small that radiation at the top surface is insignificant. The rate of change of the energy $\dot{e}$ is approximated with a Backward Euler scheme, resulting in a fully implicit, stable time integrator. The state variables are updated based on the temperature field in each iteration using Eqs. (10) and (16).

The degree of consolidation ψ is used to account for the change in geometry. As the material consolidates from a porous powder to a dense melt, the geometry shrinks considerably. We account for the consolidation/shrinkage by assuming a form of the deformation gradient $\boldsymbol{F}$ where $\det(\boldsymbol{F})$ is equal to the local volume ratio associated with consolidation Eq. (27). We assume that the consolidation is primarily driven by gravity in the x_3 direction (see Fig. 1), and thus, the deformation gradient is only different from the identity in the F_{33} component, which is set $F_{33} = \det(\boldsymbol{F})$.

The non-linear, finite element discretized form of Eq. (32) is solved in Albany using various components from the Trilinos multiphysics code development framework [28]. We use the Library of Continuation Algorithms (LOCA), with time as the continuation variable, NOX for the Newton-based non-linear solver with the RILUK preconditioner in Ifpack2 [29], where the automatic differentiation utilities in Sacado are used to compute the Jacobian, and finally, Belos is used to iteratively solve the resulting linearized equations in each Newton iteration. In addition, we have incorporated into Albany a global energy calculation to ensure energy conservation at each step.

After the analysis, the deformed geometry accounting for the consolidation may be determined by solving a simple linear finite element system of equations for the displacement field using the assumed deformation gradient on the domain. Specifically, we solve for the displacement field $\boldsymbol{u}$ from

$$\int_{\Omega_0} (\nabla \boldsymbol{u} - \boldsymbol{F} - \boldsymbol{I}) \cdot \nabla \boldsymbol{v} \, d\Omega_0 = 0 \tag{33}$$

where $\boldsymbol{v}$ is an arbitrary weighting vector field. We only solve in the powder region, where all the consolidation takes place. For a boundary condition, we set the displacement field to zero at the substrate. Since we ignore the effect of surface

tension, the shape of the melted powder above the substrate will not be properly captured, but the width and depth of the melt region should be accurate, as will be shown in the next section.

We have integrated Simmetrix [30] meshing tools with the Albany analysis code in memory for the finite element analysis, which allows scalable computations on parallel high performance computing platforms. To save computational time and space, Simmetrix tools for unstructured meshing were integrated with the Albany analysis code so that the mesh in the vicinity of the laser beam, where the temperature gradients are very high, is highly refined, while further away from the laser beam the mesh is coarse. Because the laser path is known a priori, we refine the mesh along the entire laser path initially. In the future, we will include adaptivity that will allow for the mesh to evolve as the laser beam moves and as the material consolidates.

4 Results and discussion

To demonstrate the model and finite element implementation, we compare our simulations to simulations and experiments of a single laser track presented in Gusarov et al. [7], where we investigate the effect of consolidation on the predictions of the temperature field and melt pool geometry. In addition, we present results for a more realistic spiral path. For each example, we model a domain with lateral dimensions of $w_1 = w_2 = 500\,\mu\text{m}$ and a substrate depth of $d_s = 150\,\mu\text{m}$ for a total depth (powder and substrate) of $200\,\mu\text{m}$ (see Fig. 1). The processing parameters used in the simulations on stainless steel 316L are given in Table 3, where T_0 is the initial temperature of the domain. Yadroitsev et al. [31] have studied the effects of processing parameters such as scanning speed and laser power on single track formation. In that study, the authors have provided the optimal range of processing parameters such that instabilities like distortion, irregularities and balling effect during a SLM process can be avoided. In our study, we present simulation results that fall within this optimal range of process parameters.

We first compare our simulation results to those presented in Gusarov et al. [7], where the effect of consolidation was not considered. Consolidation can be turned off in our model by setting the deformation gradient equal to the identity, $\boldsymbol{F} = \boldsymbol{I}$, and using Eqs. (17) and (26) for the heat source in the powder and substrate, respectively. In this case, we set the powder

porosity to be $\varepsilon_0 = 0.652$ corresponding to an optical thickness of $\lambda = 2$, and we model a laser with constant power, $P = 30\,\text{W}$, traveling at scan speeds of 12, 16, 20 and 24 cm/s. We treat one edge of the domain as a symmetry boundary and model half of the laser beam traveling along the top surface on this edge. The unstructured mesh is shown in Fig. 5, where the mesh is refined along the edge where the laser beam travels. The mesh has approximately 295 K linear tetrahedral elements and 60 K degrees of freedom. Because the temperature gradients are very high in SLM, we can allow for a larger phase interface thickness δ without significantly affecting the simulation results. The interface thickness relates to the required mesh refinement in the vicinity of the melt interface. In the SLM simulations, we set $(T_l - T_s)/A = 150\,\text{K}$, which corresponds to an interface thickness of less than $20\,\mu\text{m}$. The laser center moves along the edge $x_2 = 0$ from $x_1 = 100\,\mu\text{m}$ to $x_1 = 250\,\mu\text{m}$, which is sufficient to reach a steady-state temperature field and melt pool. We obtain peak temperature results for these simulations within 3.6% of the results presented in [7]. We performed these simulations with a time step of $\Delta t = 1\,\mu\text{s}$, which is an order of magnitude higher than required in Gusarov et al. [7] ($\Delta t = 0.1\,\mu\text{s}$), who use an explicit integration scheme and solve at steady-state on a spatial domain. We find that we can further increase the time step to $\Delta t = 50\,\mu\text{s}$, with little loss of accuracy, as shown in the next examples.

To investigate the effect of consolidation on the simulation predictions, we compare simulation results including the effect of consolidation to results not including the effect. The initial porosity is assumed to be $\varepsilon_0 = 0.6$ corresponding to an optical thickness of $\lambda = 2.5$. We model a laser with constant power, $P = 30\,\text{W}$, traveling at scan speeds of 10 cm/s. Figure 6 shows the temperature at the top surface along the center-line of the laser path, which includes the peak temperature. The melt temperature (1700 K) and the vaporization temperature (3300 K) are also shown in Fig. 6. We see that including consolidation in the simulation considerably reduces the peak temperature and the size of the melt pool. In Gusarov et al. [7], they find that they must use a reduced power in the simulations of 30 W as compared to the nominal experimental laser power of 50 W in order to obtain a melt pool comparable to that observed experimentally. The effect of consolidation may be the primary reason for the discrepancy, as considerably less power is absorbed when the material melts and consolidates. Furthermore, we see that the model ignoring the effect of consolidation predicts a significant region above the vaporization temperature, while the simulation that takes into account the effect of consolidation does not predict the peak temperature exceeding the vaporization temperature. Exceeding the vaporization temperature can lead to porosity, due to boiling, and keyhole defects, and thus, the simulation model should be able to accurately characterize the region above the vaporization temperature.

Table 3 Parameters used in the simulations of SLM of stainless steel 316L shown here

ε_0	D (μm)	d_p (μm)	R (μm)	ρ	f	T_0 (K)
0.652, 0.600	20	50	60	0.7	1	300

Fig. 5 Mesh of powder-substrate model, where the mesh is more refined in the vicinity of the laser
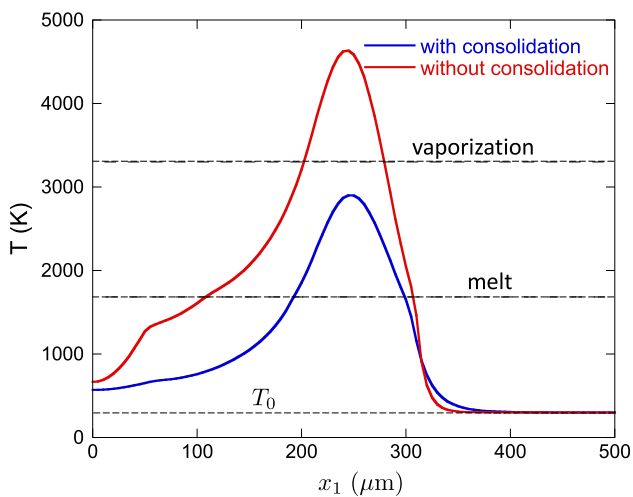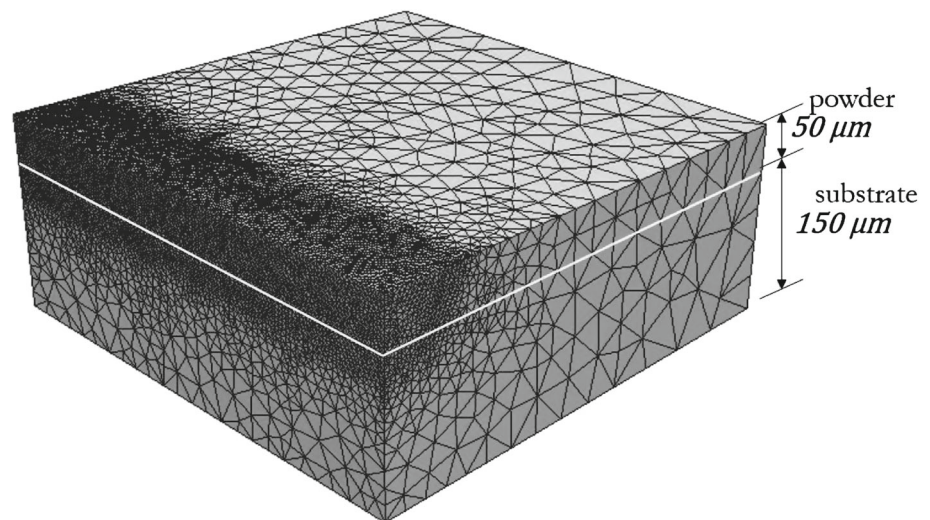

Fig. 6 Temperature profiles at the top surface of the powder along the laser path showing the decrease in temperature while considering consolidation using a 30 W laser

Next, we simulate an experimental test case with the full laser power of $P = 50$ W and compare the simulation predictions for the melt pool width and depth to the measured values in Gusarov et al. [7]. We consider the case with a scan speed of 16 cm/s. Figure 7a shows the temperature field on the top surface and Fig. 7b shows the phase parameter ϕ, where $\phi = 1$ is associated with the melt pool is shown in red, and $\phi = 0$ is associated with either unmelted powder or re-solidified, dense material (behind the melt zone). Figure 7c shows a cross-section view, again showing the phase parameter ϕ. We can see the width w_m and depth d_m of the melt zone in the substrate as well as the melted and consolidated powder above the substrate. The predicted width and depth of the melt zone from the simulation are $w_m = 92$ mm and $d_m = 23$ mm, compared to the experimental measurements

of $w_m = 100$ mm and $d_m = 22$ mm reported in [7]. Thus, we obtain excellent agreement with experimental values from the literature for the substrate melt pool size. Figure 7d is a plot of the temperature along the centerline of the laser path on the top surface and at the powder–substrate interface. We can see that the simulation predicts a small zone, directly under the laser at the top surface, where the material is above the vaporization temperature. The width of the melt zone at the top is only slightly longer than at the interface with the substrate.

Lastly, we model a *spiral in* pattern to melt a region on the interior of the simulation domain. In this example, we use a mesh that is uniformly refined near the top surface with approximately 585 K linear tetrahedral elements and 116 K nodes, and we set the time step to $\Delta t = 50\,\mu$s. The scan speed set at 16 cm/s, and three values for the laser power are considered $P = 20, 30$ and 50 W. The simulation results for a square spiral pattern at an instant in time are shown in Fig. 8. The simulations were performed on 2 compute nodes, each node with 8-2.3GHz Opteron processors and 16 GB of 1333 MHz DDR3 ECC memory and took only about 0.5 h each. For a 50 W laser (Fig. 8c) the consolidated melted region (red, $\psi = 1$) shows the complete coverage of the interior region at the instant of the simulation. It is important for the powder to be fully melted and consolidated all the way to the substrate to avoid interior porosity and defects. Thus, we also show the melted and consolidated region at the initial powder–substrate interface (bottom row) as well as the cross-section (middle row) of the entire model. We see that for the spiral pattern shown, the entire interior region is fully melted and consolidated in case of the 50 W laser, whereas, incomplete melting is visible for the 20 and 30 W laser powers. Internal defects arises at the corners and between the parallel passes of the pattern due to both incomplete melting and improper hatch distance. In the case of the 30 W laser, the internal
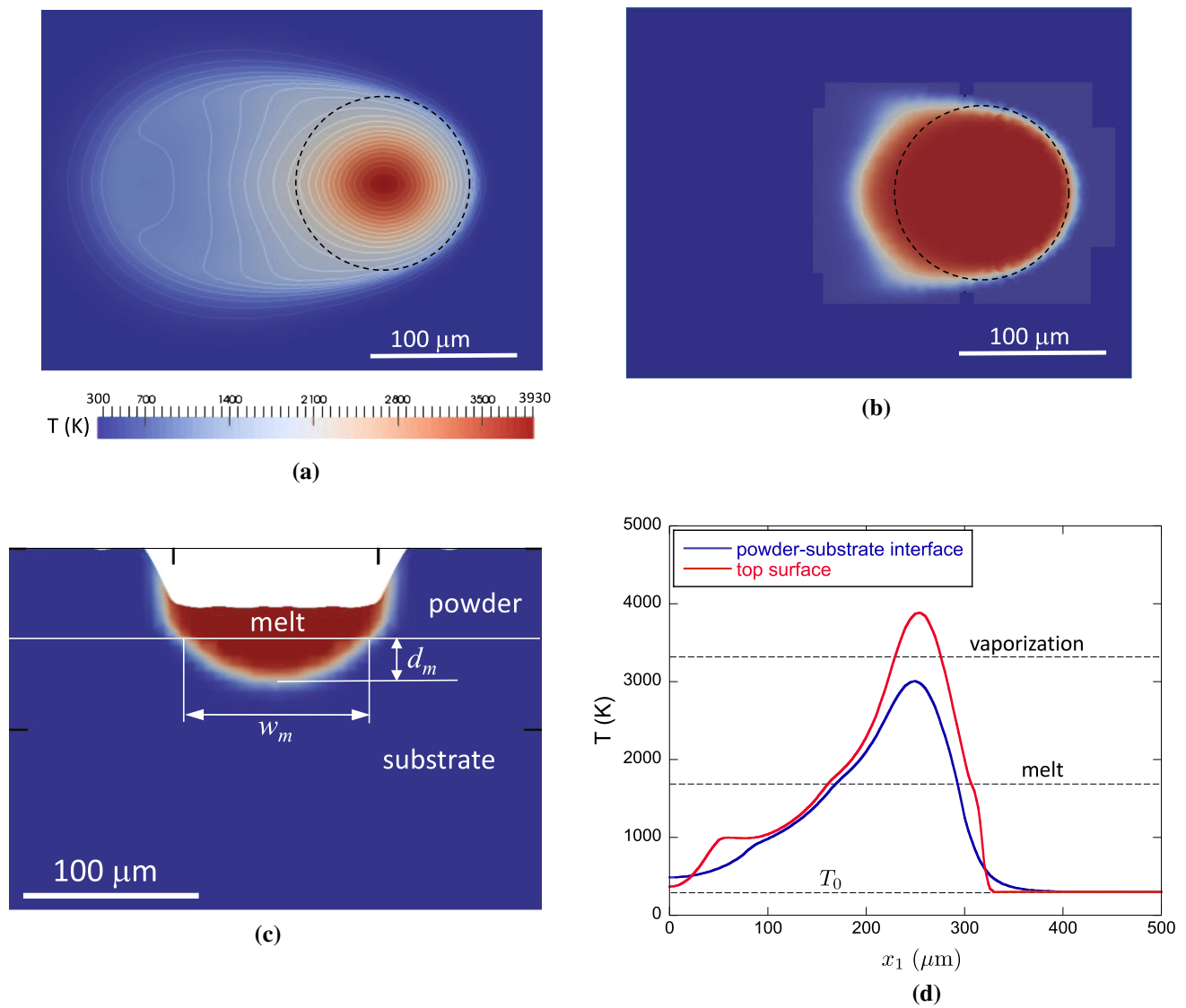
Fig. 7 Simulation results for a 50 W laser traveling at a scanning speed 16 cm/s (left to right) with a full beam radius $R = 60\,\mu$m at steady state. **a** Temperature field on the top surface of the powder; dashed line shows the outline of laser beam. **b** The phase parameter ϕ on the top surface, red is the melt pool and blue is solid either powder or re-solidified dense material. **c** Cross-section view showing the width w_m and depth d_m of the melt pool and the consolidation of the melt region. Color map is ϕ (same as in **b**). **d** Temperature profiles along the center of the laser beam on the top surface and at the powder–substrate interface. (Color figure online)

porosity at the center of the molten track is about 8%, and at the corners, the porosity is as high as 10%.

5 Conclusion

A model with two state variables to naturally capture the melting and consolidation of the powder during SLM is presented along with a transient, implicit Lagrangian finite element formulation. The model includes the effect of the consolidation, as the powder melts and becomes fully dense, on the laser power absorption. Consolidation is found to sig-

nificantly reduce the laser power absorbed into the powder as it melts and becomes fully dense. By including this effect, the model is found to accurately predict the width and depth of the melt zone in the substrate for a given laser power and scan speed. The model formulation is efficient, allowing for relatively large time steps, and is implemented in the general-purpose parallel finite element solver Albany [19], which allows for scalable parallel computing on high performance computing platforms. An example showing a spiral in pattern to melt an interior region was shown. In the examples shown, the laser power is set as constant, but the power can be easily adjust in the simulation, and other patterns can
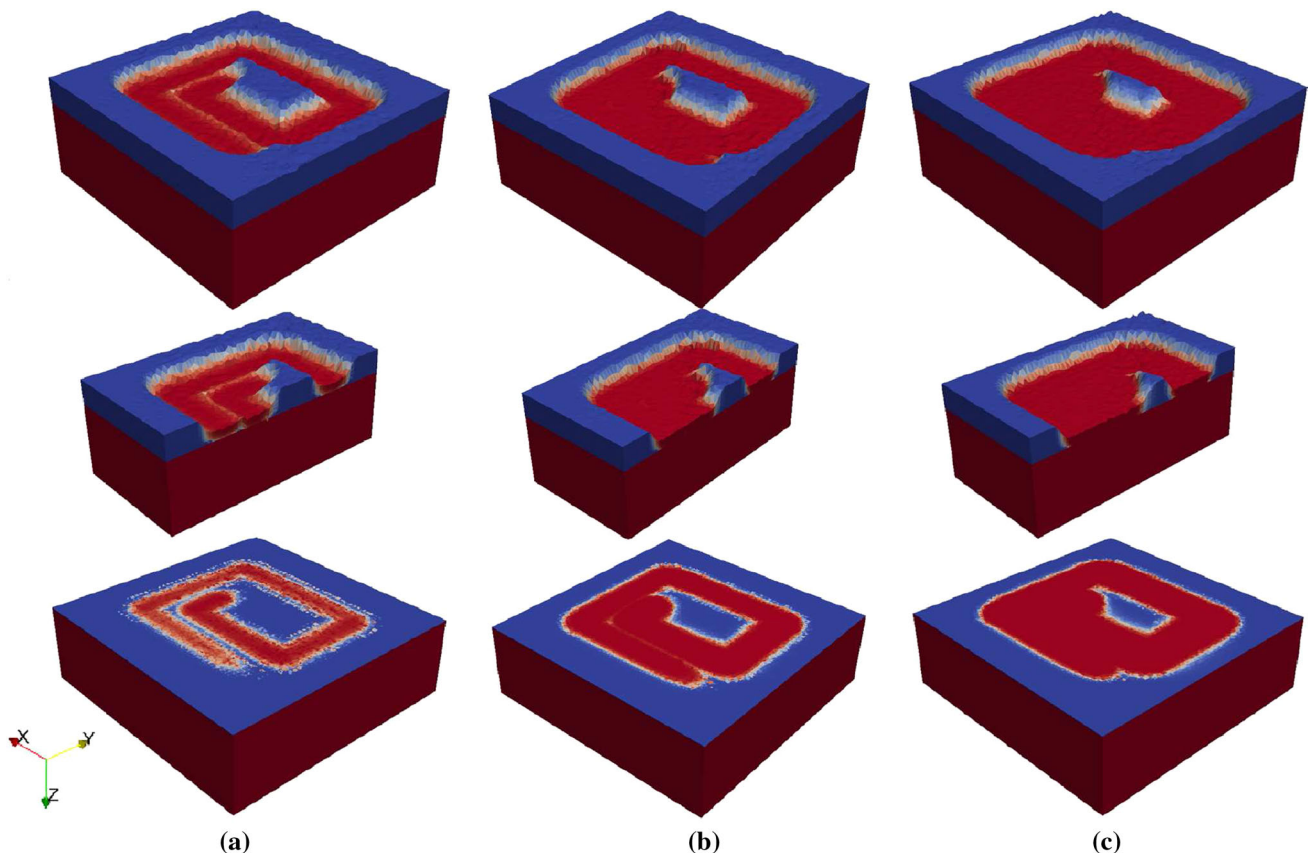
Fig. 8 Simulation results for a **a** 20 W, **b** 30 W and **c** 50 W laser traveling at a scanning speed 16 cm/s following a *spiral in* pattern. Melted consolidated region and substrate in red ($\psi = 1$) and the surrounding powder layer on top in blue ($\psi = 0$). Top row: view from top surface of powder. Middle row: cross-section view. Bottom row: section view near initial powder–substrate interface. For the 20 and 30 W laser, incomplete melting is visible at the powder substrate interface (discontinuity in red coloring) in between parallel lines and at the corners. (Color figure online)

be quickly simulated too. Because the simulations can be carried out fairly quickly, they can be conducted within an iterative learning loop [32] to determine the optimal laser power history, which is the subject of a forthcoming paper.

In addition, the model developed here is well-suited to serve as a platform for incorporating thermal–mechanical simulations and modeling multi-layer part builds. The model presented here provides the material state of melt and consolidation everywhere and the current part geometry (consolidated, non-powder material), which can be computed at the end of each layer as shown in this work. The mechanical response, thermal shrinkage and associated stress, is not expected to significantly impact the thermal analysis, so the coupling is one-way. Thus, the temperature and state variable history would be the input to a thermal–mechanical analysis that could be performed after the thermal analysis for each layer. The material properties would naturally depend on the temperature and state variables. For example, the elastic modulus and flow stress can be expressed in terms of the temperature and porosity (related to consolidation state variable). Because Albany is a generic finite element solver, adding the mechanical analysis is relatively straight-forward. After thermal and stress analyses, the model could be re-initiated for modeling the next layer with a new powder layer added and a new mesh that follows the new part–powder interface on the interior.

References

1. Bourell DL, Leu MC, Rosen DW (eds) (2009) Roadmap for additive manufacturing: identifying the future of freeform processing. University of Texas, Austin
2. Markl M, Körner C (2016) Multiscale modeling of powder bed-based additive manufacturing. Annu Rev Mater Res 46:93–123
3. Körner C, Bauereiß A, Attar E (2013) Fundamental consolidation mechanisms during selective beam melting of powders. Modell Simul Mater Sci Eng 21:085011
4. Khairallah SA, Anderson A (2014) Mesoscopic simulation model of selective laser melting of stainless steel powder. J Mater Process Technol 214:2627–2636
5. Khairallah SA, Anderson A, Rubenchik A, King WE (2016) Laser powder-bed fusion additive manufacturing: physics of complex melt flow and formation mechanisms of pores, spatter, and denudation zones. Acta Mater 108:36–45
6. Protasov CE, Khmyrov RS, Grigoriev SN, Gusarov AV (2017) Selective laser melting of fused silica: interdependent heat transfer and powder consolidation. Int J Heat Mass Transf 104:665–674
7. Gusarov AV, Yadroitsev I, Bertrand P, Smurov I (2009) Model of radiation and heat transfer in laser–powder interaction zone at selective laser melting. J Heat Transf 131(7):072101-1–072101-10
8. Verhaeghe F, Craeghs T, Heulens J, Pandelaers L (2009) A pragmatic model for selective laser melting with evaporation. Acta Mater 57:6006–6012
9. Hodge NE, Ferencz RM, Solberg JM (2014) Implementation of a thermomechanical model for the simulation of selective laser melting. Comput Mech 54:33–51
10. Yan W, Ge W, Smith J, Lin S, Kafka OL, Lin F, Liu WK (2016) Multi-scale modeling of electron beam melting of functionally graded materials. Acta Mater 115:403–412
11. Dai K, Shaw L (2006) Parametric studies of multi-material laser densification. Mater Sci Eng 430:221–229
12. Ma L, Bin H (2007) Temperature and stress analysis and simulation in fractal scanning-based laser sintering. Int J Adv Manuf Technol 34:898–903
13. Hussein A, Hao L, Yan C, Everson R (2013) Finite element simulation of the temperature and stress fields in single layers built without-support in selective laser melting. Mater Des 52:638–647
14. Paul R, Anand S, Gerner F (2014) Effect of thermal deformation on part errors in metal powder based additive manufacturing processes. J Manuf Sci Eng Trans ASME 136:031009
15. Denlinger ER, Irwin J, Michaleris P (2014) Thermomechanical modeling of additive manufacturing large parts. J Manuf Sci Eng Trans ASME 136:061007
16. Yu J, Lin X, Ma L, Wang J, Fu X, Chen J, Weidong H (2011) Influence of laser deposition patterns on part distortion, interior quality, and mechanical qualities by laser solid forming. Mater Sci Eng A 528:1094–1104
17. King WE, Barth HB, Castillo VM, Gallegos GF, Gibbs JW, Hahn DE, Kamath C, Rubenchik AM (2014) Observation of keyhole-mode laser melting in laser powder-bed fusion additive manufacturing. J Mater Process Technol 214:2915–2925
18. Xiao B, Zhang Y (2007) Analysis of melting of alloy powder bed with constant heat flux. Int J Heat Mass Transf 50:2161–2169
19. Salinger AG, Bartlett RA, Bradley AM, Chen Q, Demeshko IP, Gao X, Hansen GA, Mota A, Muller RP, Nielsen E, Ostien JT, Pawlowski RP, Perego M, Phipps ET, Sun W, Tezaur IK (2016) Albany: using component-based design to develop a flexible, generic multiphysics analysis code. Int J Multiscale Comput Eng 14(4):415–438
20. Wang S-L, Sekerka RF, Wheeler AA, Murray BT, Coriell SR, Braun RJ, McFadden GB (1993) Thermodynamically-consistent phase-field models for solidification. Physica D 69:189–200
21. Davis JR (ed) (1994) Stainless steels. ASM specialty handbook. ASM, Materials Park
22. Song B, Dong S, Liao H, Coddet C (2012) Process parameter selection for selective laser melting of Ti_6Al_4V based on temperature distribution simulation and experimental sintering. Int J Adv Manuf Technol 61:967974
23. Antony K, Arivazhagan N, Senthilkumaran K (2014) Numerical and experimental investigations on laser melting of stainless steel 316l metal powders. J Manuf Process 16:345–355
24. Mazumder J, Steen WM (1980) Heat transfer model for cw laser material processing. J Appl Phys 51(2):941–947
25. Cremers DA, Lewis GK, Korzekwa DR (1991) Measurement of energy deposition during pulsed laser welding. Weld J 40(7):159-s–167-s
26. Rai R, Elmer JW, Palmer TA, DebRoy T (2007) Heat transfer and fluid flow during keyhole mode laser welding of tantalum, Ti_6Al_4V, 304L stainless steel and vanadium. J Phys D Appl Phys 40:5753–5766
27. Hansen G Albany project website. https://github.com/gahansen/albany/wiki
28. Heroux MA, Bartlett RA, Howle VE, Hoekstra RJ, Hu JJ, Kolda TG, Lehoucq RB, Long KR, Pawlowski RP, Phipps ET, Salinger AG, Thornquist HK, Tuminaro RS, Willenbring JM, Williams A, Stanley KS (2005) An overview of the trilinos project. ACM Trans Math Softw 31(3):397–423
29. Prokopenko A, Siefert CM, Hu JJ, Hoemmen M, Klinvex A (2016) Ifpack2 users guide 1.0. Technical report SAND2016-5338, Sandia National Labs, 2016
30. Beall M, Simmetrix, Inc. website. http://www.simmetrix.com/
31. Yadroitsev I, Gusarov A, Yadroitsava I, Smurov I (2010) Single track formation in selective laser melting of metal powders. J Mater Process Technol 210:1624–1631
32. Bristow DA, Tharayil M, Alleyne AG (2006) A survey of iterative learning control. IEEE Control Syst 26(3):96–114